Green Chemistry

COMMUNICATION

View Article Online
View Journal

Cite this: DOI: 10.1039/c5gc01588j

Received 13th July 2015,
Accepted 14th October 2015

DOI: 10.1039/c5gc01588j

www.rsc.org/greenchem

Synthesis of Ni-based co-catalyst functionalized W:$BiVO_4$ nanofibers for solar water oxidation†

Ki Ro Yoon,‡ Jong Wan Ko,‡ Doo-Young Youn, Chan Beum Park* and Il-Doo Kim*

We report on the synthesis of highly porous, 1-D tungsten-doped $BiVO_4$ nanofibers (W:$BiVO_4$ NFs). To facilitate photocatalysis, we introduced nickel nanoparticles (NiO_x NPs) as co-catalysts on the surface of W:$BiVO_4$ NFs. The outstanding water oxidation performance of the NiO_x NP-functionalized W:$BiVO_4$ NFs was obtained through (i) the control of polymers/precursors to achieve porous W:$BiVO_4$ NFs (for highly increased surface area), (ii) the control of the tungsten-doping level (for fast charge transfer), and (iii) the optimization of the loading amounts of NiO_x NPs (for efficient charge pathway suppression of charge recombination).

Harnessing solar energy has recently attracted much attention due to the increased importance of environmental and energy issues.[1] In particular, the photolysis of water using photocatalysts, so called artificial photosynthesis, has been receiving great attention in terms of the direct and efficient solar energy conversion system to produce O_2 and H_2 as chemical fuels.[2] The effectiveness of water splitting using photocatalysts is determined by the utilization of visible light of the solar spectrum, capacity of the harvested light to generate charge carriers, and the extent of charge separation and transfer.[3] Thus, the selection of semiconducting photocatalyst materials with an appropriate band position, bandgap energy, and long-lived stability is critical for the viable water splitting system.[4]

Bismuth vanadate ($BiVO_4$) is one of most promising photocatalysts because of its small band gap energy of 2.4–2.6 eV in the monoclinic-scheelite phase, the sufficient valence band position for water oxidation, and superior chemical stability.[5] For these reasons, $BiVO_4$ has been widely studied as anode materials for photoelectrochemical cells[6] and as suspended photocatalysts for water oxidation or a dye degradation system[7] under visible light irradiation. However, $BiVO_4$ has formidable challenges such as the low charge mobility and the fast charge recombination of an electron–hole pair (EHP), which provide low energy conversion efficiency.[8] To overcome its inherent charge separation and suppress the charge recombination of EHPs, doping is widely used to increase the charge lifetime without band gap alteration.[9] Metal doping such as Mo and W substituting for V sites in $BiVO_4$ can improve water oxidation efficiency by increasing the major carrier density.[10] In addition, heterogeneous catalysts or co-catalysts were introduced to improve the photocatalytic activities of $BiVO_4$.[4] Thus far, noble metals including Pt, Pd, Ag, and Au have been widely used as electron sinks for efficient charge separation.[11] Transition metal complexes or oxides (*e.g.*, Ni–Bi, Co–Pi, CoO, Co_3O_4, FeOOH and TiO_2) have been extensively explored as co-catalysts to facilitate the reaction of water oxidation.[6b,10b,12] Nickel or nickel oxides (NiO_x, $0 < x < 1$) have also been known as great water oxidation catalysts since the early stage of water splitting studies. NiO_x have been applied to photocatalysts such as Ta_2O_5, $SrTiO_3$, and $BaLa_4Ti_4O_{15}$ as co-catalysts for improving the water oxidation reaction.[13] It raises a motivation that we can integrate metal doped $BiVO_4$ and NiO_x for the synergistic effect on photocatalytic reaction.

As widely known, low dimensional materials have various advantages in different technologies due to their mechanical, optical, and electrical properties and the increased specific surface area compared with those of the bulk materials.[14] Many research efforts have been made to develop low dimensional or nano-sized $BiVO_4$ as photocatalysts.[15] In particular, one dimensional (1-D) nanomaterials, such as nanowires or nanofibers, were employed in $BiVO_4$ for photocatalysis due to their enlarged surface area and unique charge transfer kinetics along the 1-D direction, but most of the synthetic routes have been limited by the use of solution-based processes, such as hydrothermal or solvothermal methods.[16] Recently, Y. Cheng *et al.* reported the preparation of $BiVO_4$ fibers by electrospinning,[17] but their work was mainly focused on the morphological study according to the calcination temperature and their photocatalytic dye-degradation performance. Thus, the

Department of Materials Science and Engineering, Korea Advanced Institute of Science and Technology (KAIST), 335 Science Road, Yuseong-gu, Daejeon 305-701, Republic of Korea. E-mail: parkcb@kaist.ac.kr, idkim@kaist.ac.kr; Fax: +82 42 350 3310; Tel: +82 42 350 3340

† Electronic supplementary information (ESI) available: Experimental details and supporting data of SEM, TEM, XRD, EDS, cyclic voltammetry, XPS, and UV-visible spectra. See DOI: 10.1039/c5gc01588j

‡ These authors contributed equally to this work.

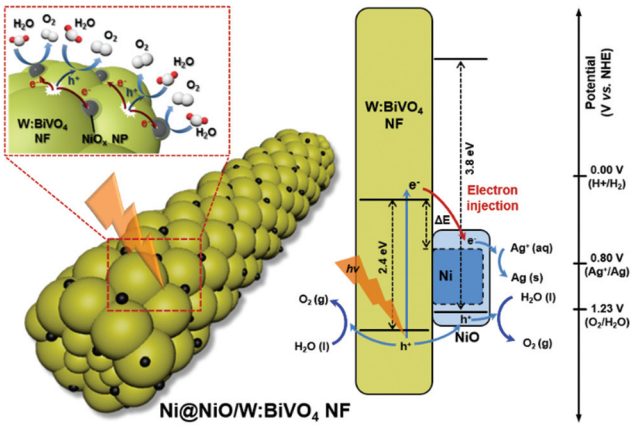

Scheme 1 Schematic illustration of the proposed water oxidation reaction using Ni@NiO/W:$BiVO_4$ NFs under visible light irradiation.

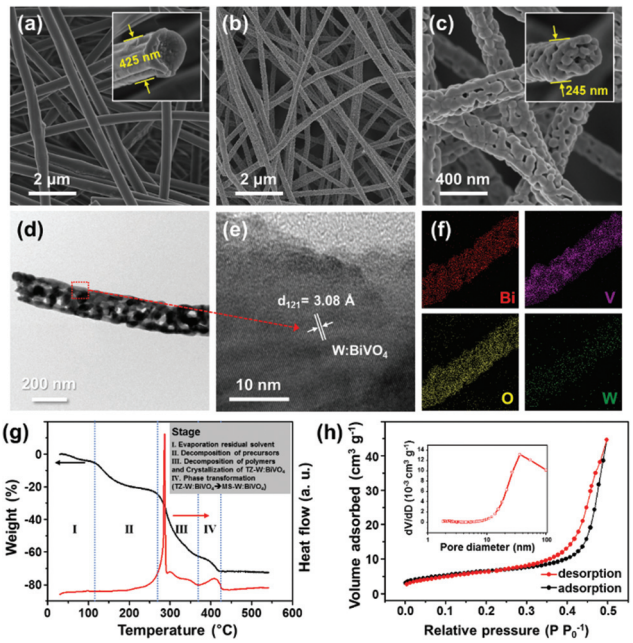

Fig. 1 SEM images of (a) as-spun polymer/precursor fibers (inset is a cross-section image of as-spun fibers), crystallized W:$BiVO_4$ NFs with (b) low and (c) high magnification. (d) TEM image of W:$BiVO_4$ NFs and (e) HRTEM image of the red box from (d). (f) Element mapping of W:$BiVO_4$ NFs. (g) TG/DSC curves of W:$BiVO_4$ NFs (TG curve: black, DSC curve: red, heating range: 30–550 °C with a rate of 5 °C min^{-1}). (h) N_2 adsorption–desorption isothermal graph and BJH pore-size distribution (inset) of W:$BiVO_4$ NFs. The representative W:$BiVO_4$ is 1 at% W doped $BiVO_4$, substituting the V sites ($BiV_{0.99}W_{0.01}O_4$).

rational design of efficient photocatalysts by introducing a co-catalyst or doping into $BiVO_4$ is highly desired.

Herein, we report on the synthesis of W-doped $BiVO_4$ nanofibers (W:$BiVO_4$ NFs) using the electrospinning process, the most facile and versatile route for producing polycrystalline 1-D nanomaterials. Furthermore, we introduced Ni nanoparticles (NPs) as co-catalysts, which are immobilized on the outer surface of W:$BiVO_4$ NFs. Core Ni–shell NiO (Ni@NiO) NPs were functionalized on W:$BiVO_4$ NFs (hereafter, NiO@Ni/W:$BiVO_4$ NFs) after mixing and annealing under an Ar atmosphere. The overall preparation of the NiO@Ni/W:$BiVO_4$ NFs is described in the ESI (Experimental details and Fig. S1†). The improved photocatalytic water oxidation characteristics of the Ni@NiO/W:$BiVO_4$ NFs were investigated in comparison with those of pristine, fully oxidized NiO- and Pt-loaded W:$BiVO_4$ NFs. Scheme 1 shows the schematic illustration of Ni@NiO/W:$BiVO_4$ NFs and the proposed reaction as a photocatalyst for water oxidation. When W:$BiVO_4$ NFs are irradiated under visible light, the photogenerated electrons in W:$BiVO_4$ NFs readily transfer to the Ni core as an electron sink, while the photogenerated holes can take part in the water oxidation reaction on the surface of W:$BiVO_4$ NFs, simultaneously. Furthermore, oxidized Ni elements also act as additional water oxidation sites where residual holes from W:$BiVO_4$ NFs are transferred to the outer part of NiO. We conclude that the outstanding performance of the Ni@NiO/W:$BiVO_4$ NFs was mainly attributed to the unique core–shell structure of Ni@NiO providing bi-functional effects on the W:$BiVO_4$ NFs in a synergistic manner. This work offers a simple preparation method for the integrated materials including 0-D Ni NPs and 1-D W:$BiVO_4$ NFs and demonstrates the effect of co-catalysts explained by the band structures of metals and/or metal oxides for photocatalytic water oxidation.

The morphologies of the electrospun W:$BiVO_4$ NFs were examined using a scanning electron microscope (SEM) and a transmission electron microscope (TEM). As-spun composite fibers including inorganic precursors $(Bi(NO_3)_3{\cdot}5H_2O$, $VO(AcAc)_2$, and $W(OC_2H_5)_5$ with an atomic ratio of Bi : V : W = 50 : 49 : 1) and two polymers (polyvinylpyrrolidone (PVP) and polyvinyl-acetate (PVAc)) exhibited a continuous 1-D structure with a smooth surface and a uniform diameter of ~400 nm (Fig. 1a). After calcination at 450 °C in air, polycrystalline W:$BiVO_4$ NFs were obtained through the decomposition of the polymers and crystallization of W:$BiVO_4$. The morphology of the W:$BiVO_4$ NFs was significantly influenced by the matrix polymers that were used as sacrificial templates during the electrospinning process (Fig. S2†). When a PVP polymer was solely used, the calcined W:$BiVO_4$ NFs consisted of large grains and dense structures without any pores. On the other hand, W:$BiVO_4$ NFs prepared with only PVAc containing solution exhibited numerous pores on the surface, but the 1-D nanofiber structure collapsed. This is attributed to the phenomenon that the incompatibility of the PVAc and metal precursors stimulated a highly porous structure, but the lower molecular weight of PVAc did not maintain the 1-D nanofiber morphology. The use of the solution with rational mixing of two polymers, *i.e.*, PVP and PVAc with a weight ratio of 1 : 1, provided the successfully synthesized W:$BiVO_4$ NFs with a highly porous and 1-D elongated morphology (Fig. 1b and c). The morphology controlled W:$BiVO_4$ NFs consisted of nano-sized grains (30–80 nm) and reduced diameters of ~250 nm due to the volumetric densification of inorganic compounds

and removal of residual solvents and polymers during calcination. The voids of the fibers were clearly observed in the TEM image (Fig. 1d), and the magnified image shows that the interplanar distance of the domain is 3.08 Å corresponding to the (121) plane of monoclinic-scheelite type $BiVO_4$ (Fig. 1e). As shown in energy-dispersive X-ray spectroscopy (EDS) (Fig. S3†) and elementary mapping (Fig. 1f), the representative W:$BiVO_4$ NFs have W atoms around 1 at% of the W doping level and they are well distributed into the overall W:$BiVO_4$ composite. The synthetic process of porous W:$BiVO_4$ NFs was investigated using a thermogravimetric analyzer and differential scanning calorimetry (TGA/DSC) (Fig. 1g). The specific surface area of the W:$BiVO_4$ NFs was investigated using the Braunauer–Emmett–Teller (BET) method (Fig. 1h). The BET surface area of W:$BiVO_4$ NFs is 18.95 $m^2\ g^{-1}$, which is relatively higher than that of W:$BiVO_4$ particles (2.88 $m^2\ g^{-1}$) prepared by the conventional solid-state reaction. The morphologies of W:$BiVO_4$ NFs were largely affected by the calcination temperature (Fig. S4†). The temperature dependence of the BET surface area and crystalline size was measured and calculated as shown in Fig. S5 and Table S1.† In brief, the BET surface area drastically decreased as the calcination temperature increased due to the huge grain growth of W:$BiVO_4$. The inset of Fig. 1h shows that the mesopores between 10–100 nm are attributed to many voids distributed on the surface of the nanofibers. In our TGA/DSC analysis, the first minor weight loss below 120 °C corresponded to the evaporation of the volatile component. The weight loss in the range of 120–280 °C was attributed to the decomposition of intermolecular bonding of inorganic precursors and PVAc (T_g = ~30 °C). The significant weight loss above 280 °C was mainly due to the decomposition of PVP (T_g = 150–180 °C) and residual PVAc, and no weight loss was found above 410 °C. According to the TGA curve, the porous 1-D structure was formed by the removal of the volatile matters, inorganic precursor groups, PVAc and PVP. The DSC curve showed the first exothermal peak around 285 °C, which indicates the crystallization of tetragonal-zircon phased W:$BiVO_4$. The additional exothermal peak around 410 °C means that phase transformation into monoclinic-scheelite occurs, which has the highest photocatalytic activity among the three types of crystal phased $BiVO_4$ (monoclinic-scheelite, tetragonal-scheelite, and tetragonal-zircon type).[5b]

Ni NPs were synthesized by a modified polyol method.[18] The as-prepared Ni NPs have a globular shape, which has (111) crystallographic planes of the Ni metal (Fig. 2a, b). Ni NPs have a broad size distribution of about 2–10 nm and an average diameter of 6.8 nm (Fig. 2c). Ni NP loaded W:$BiVO_4$ NFs were prepared with different loading levels (0.01, 0.1, 0.2, and 1 wt%). Among them, 0.1 wt% Ni loaded W:$BiVO_4$ NFs were characterized by SEM and TEM analysis as the representative samples due to their outstanding catalytic activity (Fig. 2d–f). As shown in Fig. 2d, small Ni NPs were attached to the surface of the W:$BiVO_4$ NFs (red dashed circles). A high resolution TEM image shows that the attached Ni NPs are surrounded by a thin layer with an estimated thickness of ~1.5 nm. The ring patterns corresponded to (110), (121), (220),

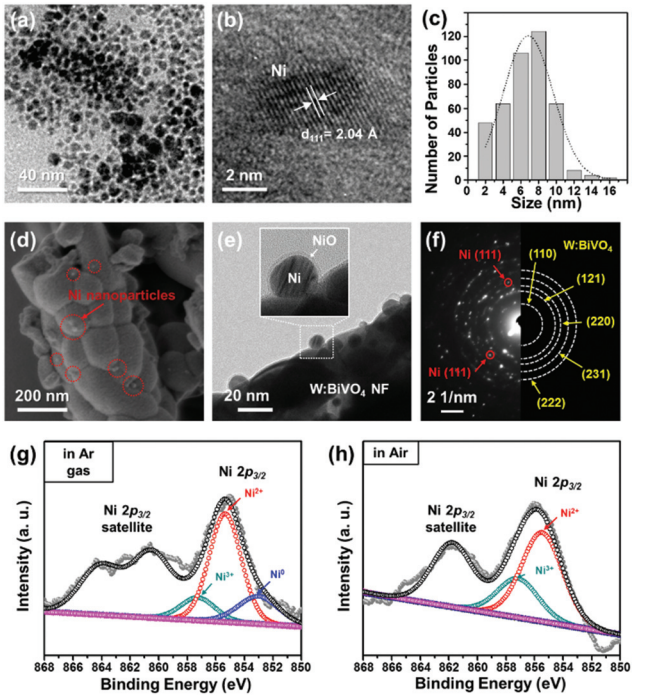

Fig. 2 TEM images of synthesized (a) Ni NPs and (b) their lattice fringes. (c) The size distribution of synthesized Ni NPs measured from (a). (d) SEM image of 0.1 wt% Ni@NiO loaded W:$BiVO_4$ NFs (0.1Ni@NiO/W:BiVO4 NFs). Red circle indicates Ni NPs. (e) TEM image of 0.1Ni@NiO/W:$BiVO_4$ NFs and (f) corresponding SAED patterns. High resolution XPS spectra of Ni 2p orbitals of (g) Ni@NiO/W:$BiVO_4$ NFs and (h) 0.1 wt% NiO loaded W:$BiVO_4$ NFs (0.1NiO/W:$BiVO_4$ NFs).

(231), and (222) planes of W:$BiVO_4$ and the discrete dots represented the (111) plane of Ni (Fig. 2f). Even though Ni elements were hardly identified with XRD patterns due to their small amounts, all the samples displayed identical diffraction patterns of monoclinic-scheelite phased $BiVO_4$ (PDF#14-0688) (Fig. S6†). To identify the oxidation state of Ni NPs, X-ray photoelectron spectroscopy (XPS) analysis was carried out for Ni NP loaded W:$BiVO_4$ NFs (Fig. 2g and h). The survey scans of XPS showed that binding energies of Ni $2p_{3/2}$ are placed in the range of 850–870 eV (Fig. S7†). As shown in Fig. 2g, for Ni NP loaded W:$BiVO_4$ NFs in Ar gas, the distinctive peaks were detected at 852.85, 855.56, and 857.25 eV, matched with nickel metals, Ni^{2+} and Ni^{3+}.[19] It is ambiguous to classify the oxidation states of NiO and $Ni(OH)_2$.[20a] In the cyclic voltammetry (CV) analysis (Fig. S8†), a Ni^{3+}/Ni^{2+} redox wave for a NiOOH/$Ni(OH)_2$ redox couple[20] does not exist, which means that the Ni^{2+} state originated from NiO which has been known for the water oxidation catalyst. The composition of Ni was 28 at%, whereas those of NiO and Ni_2O_3 were 59 and 13 at%, respectively. It can be concluded that the surfaces of the Ni NPs were partially oxidized during the drying and annealing processes, resulting in the formation of NiO (shell)–Ni (core) NPs. Based on the analysis of TEM images and XPS spectra, the relative ratio of Ni/NiO was calculated to be 69 to 31 (based on Ni mol%). This proves the unique core–shell structure of Ni NPs observed in

Fig. 2e. Hereafter, the NiO (shell)–Ni (core) NP loaded W:$BiVO_4$ NFs are denoted as Ni@NiO/W:$BiVO_4$ NFs. On the other hand, Ni metals were fully oxidized to NiO after the annealing step under an air atmosphere. As shown in Fig. 2h, the fully oxidized NiO-loaded W:$BiVO_4$ (NiO/W:$BiVO_4$) NFs consisted of 79 at% of NiO and 21 at% of Ni_2O_3 without a metallic Ni state (Ni^0). These results indicate that the oxidation state of Ni NPs can be easily controlled under annealing atmospheric conditions.[13c] Pt has been known to be a good co-catalyst for water oxidation and plays the role of an electron sink.[11c] So Pt NPs were synthesized through the polyol method, having high crystallinity and diameter of 5–10 nm. The detailed preparation method was illustrated in the Experimental section. The (111) and (200) planes of Pt NPs were clearly observed by HRTEM (Fig. S9†), and 0.01, 0.1, 0.2, 1, and 10 wt% Pt NP-loaded W:$BiVO_4$ NFs were prepared in the same way for comparison. As shown in Fig. 3a, all the samples exhibited absorption properties in the visible light region (λ > 420 nm). The steep absorption profile of the spectrum in the visible region is due to the electron transition at the band edges of monoclinic-scheelite phased W:$BiVO_4$. These results implied that the considerable absorption in the visible light region would enable the effective utilization of visible light for photocatalytic water oxidation. As Ni loading on W:$BiVO_4$ NFs increased, the absorption of the light in a high wavelength region (λ > 500 nm) also increased and the color of the powder became darker (Fig. S10†). In brief, some portion of the light is blocked due to the shadowing effect by Ni or Pt NPs on the surface of W:$BiVO_4$ NFs, and other photons with insufficient energy to generate electron–hole pairs in W:$BiVO_4$ can be absorbed as phonons.[3a] The optical bandgap energy of each sample was calculated from the Tauc plots obtained from the diffuse-reflectance spectra. The bandgap energies of pristine W:$BiVO_4$ NFs and NiO/W:$BiVO_4$ NFs were 2.53 eV, and Pt/W:$BiVO_4$ NFs and Ni@NiO/$BiVO_4$ NFs were 2.52 eV. As displayed in Fig. S11,† W:$BiVO_4$ particles had bandgap energy of 2.41 eV, which is smaller than those of W:$BiVO_4$ NFs.

Photocatalytic water oxidation tests of W:$BiVO_4$ particles, pristine, NiO-, Pt-, and Ni@NiO-loaded W:$BiVO_4$ NFs were carried out in an aqueous solution containing silver nitrate ($AgNO_3$, 50 mM), as an electron acceptor, under visible light irradiation (λ > 420 nm). The photocatalyst samples (30 mg) were dispersed in a solution (30 mL) with magnetic stirring in a gas-closed circulation system. To optimize the doping level of W in W:$BiVO_4$, the photocatalytic water oxidation tests of W:$BiVO_4$ NFs were carried out with different W contents, *i.e.*, $BiV_{1-x}W_xO_4$, x = 0, 0.1, 0.5, 1, 2, 4, and 8. $BiV_{99}W_1O_4$ NFs showed the highest performance (Fig. S12†), which corresponds to the previous results.[10d,11b] In brief, the introduction of W gave several advantages in photocatalytic activities such as (i) generation of additional electrons resulting in the increased electronic conductivity; (ii) a local internal field aroused from the higher formal electron charge of W^{6+} compared to that of V^{5+} resulting in efficient charge separation; and (iii) an increase in the charge carrier lifetime.[10b] Table S2† summarizes the photocatalytic activities of the prepared samples including pristine W:$BiVO_4$ NFs, co-catalysts (Ni@NiO, NiO, and Pt) loaded W:$BiVO_4$ NFs, and bulk W:$BiVO_4$ particles. W:$BiVO_4$ NFs exhibited approximately 2-fold higher O_2 evolution performance than that of bulk W:$BiVO_4$ particles. This enhancement in the amount of O_2 evolution is attributed to the increased reaction sites due to higher specific surface area of W:$BiVO_4$ NFs (18.95 m^2 g^{-1}) than that of W:$BiVO_4$ particles (2.88 m^2 g^{-1}). Although the enhancement of the water oxidation performance of W:$BiVO_4$ NFs does not increase in proportion to the increase in the specific surface area, it could be explained by (i) the limited light harvesting properties due to the light blocking effect during the reaction, (ii) the polycrystalline nature of the NFs introducing the recombination sites compared to that of the particles, and (iii) the consumption of electron acceptors. The photocatalytic water oxidation performance was dramatically improved in the case of Ni@NiO/W:$BiVO_4$ NFs (Fig. 3b) and 0.1Ni@NiO/W:$BiVO_4$ NFs showed the highest activity for the O_2 evolution reaction (20.79 μmol), whereas 0.1NiO/W:$BiVO_4$ evolved 7.32 μmol of O_2 gas. The gradual reduction of photocatalytic activity is attributed to the reduced Ag^+ ions, which were deposited onto the surface of W:$BiVO_4$ NFs as the reaction

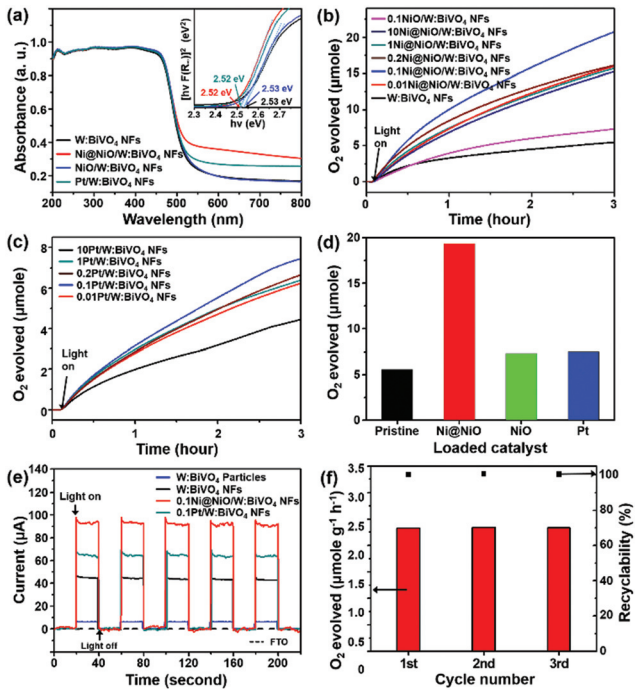

Fig. 3 (a) UV-visible diffuse-reflectance spectra and Tauc plots of $[h\nu \cdot F(R_\infty)]^2$ *versus* photon energy of the as-prepared samples (pristine, 0.1Ni@NiO-, 0.1NiO-, and 0.1Pt-loaded W:$BiVO_4$ NFs). (b) The time courses of O_2 evolution under visible light irradiation for pristine, Ni@NiO-loaded (0.01, 0.1, 0.2, 1, and 10 wt%), and 0.1NiO/W:$BiVO_4$ NFs. (c) The time courses of O_2 evolution for 0.01, 0.1, 0.2, 1, and 10 wt% Pt-loaded W:$BiVO_4$ NFs. (d) The comparison of the maximum O_2 evolution for pristine, Ni@NiO-, NiO-, and Pt-loaded W:$BiVO_4$ NFs. (e) The photocurrent density of W:$BiVO_4$ particles and NFs, 0.1 wt% Ni@NiO and Pt-loaded W:$BiVO_4$ NFs. (f) The cyclic test for 0.1Ni@NiO/W:$BiVO_4$ NFs.

proceeded.[21] In consideration of the performance of 0.1Ni@NiO/W:BiVO4 NFs, the co-catalytic effects of Ni@NiO are superior to the well known water oxidation electrocatalysts, such as Co–Pi, CoO_x, IrO_x, and RuO_x reported in the previous literature[12f] (Table S3†). The catalytic activity for O_2 evolution increased as the Ni@NiO was loaded up to 0.1 wt%. This indicates that the higher loading of NPs on the surface of W:$BiVO_4$ NFs would block the light harvesting at the host W:$BiVO_4$ catalyst, and thus the generation of charge carrier was limited.[3a] Similarly, 0.1Pt/W:$BiVO_4$ NFs showed the highest activity for O_2 evolution (7.51 μmol) compared to 0.01Pt/W:$BiVO_4$ NFs (6.24 μmol), and 1Pt/W:$BiVO_4$ NFs (7.39 μmol) (Fig. 3c). On the other hand, the activity of 0.1Pt/W:$BiVO_4$ NFs (7.51 μmol) is much lower than that of 0.1Ni@NiO/W:$BiVO_4$ NFs (19.34 μmol) (Fig. 3d). The O_2 evolution rates of the samples were also compared with the unit of mol% of Ni@NiO and Pt (Fig. S13†). The catalytic activities of all Ni@NiO/W:$BiVO_4$ NFs were higher than those of Pt/W:$BiVO_4$ NFs in all mol% ranges. As shown in Fig. 3e, the anodic photocurrent of 0.1Ni@NiO/W:$BiVO_4$ NFs was approximately 1.4 times higher than that of 0.1Pt/W:$BiVO_4$ NFs, which indicates that Ni@NiO can separate photogenerated charges in $BiVO_4$ NFs than Pt more effectively. Lastly, a life cycle test of 0.1Ni@NiO/W:$BiVO_4$ NFs without $AgNO_3$ was conducted. The composite exhibited high stability and good recyclability during the three cycles (Fig. 3f).

We suggest a mechanism based on the band structures of materials and schematic models of photocatalytic water oxidation, when the co-catalysts were applied to W:$BiVO_4$ NFs (Fig. 4). When W:$BiVO_4$ NFs are dispersed in the aqueous solution under irradiation, photogenerated EHPs in the depletion region induced by the liquid–solid junction move in the opposite direction due to the electric field.[2b] Therefore, the holes at the valence band move to the surface of the photocatalysts and take part in the water oxidation reaction, while the electrons are transferred to reduction sites on the surface of the photocatalysts. In this overall reaction, the photogenerated electrons can be easily recombined with the residual holes due to the low electron mobility as indicated by "red dot-dashed line" in Fig. 4a. This charge recombination can severely retard the photocatalytic reaction rate. In the case of NiO/W:$BiVO_4$, the band bending occurred at the interface of p-type NiO and n-type W:$BiVO_4$, then the photogenerated holes in W:$BiVO_4$ NFs can be transferred to the NiO side (Fig. 4b). NiO has also been known as an efficient water oxidation catalyst, so the transferred holes can take part in the water oxidation reaction at the NiO surface.[22] But the residual electrons are easily recombined with the holes before they are scavenged by electron acceptors. Usually, the metals facing n-type metal oxides are considered to act as electron scavenging sites during photocatalytic reactions due to their high work function value.[23] We consider that the photogenerated electrons at the surface of W:$BiVO_4$ NFs can diffuse to the Pt side quickly. Consequently, the imbalance between the densities of electrons and holes near the surface decelerates the charge recombination rate in the W:$BiVO_4$ NFs, thus water oxidation properties were improved

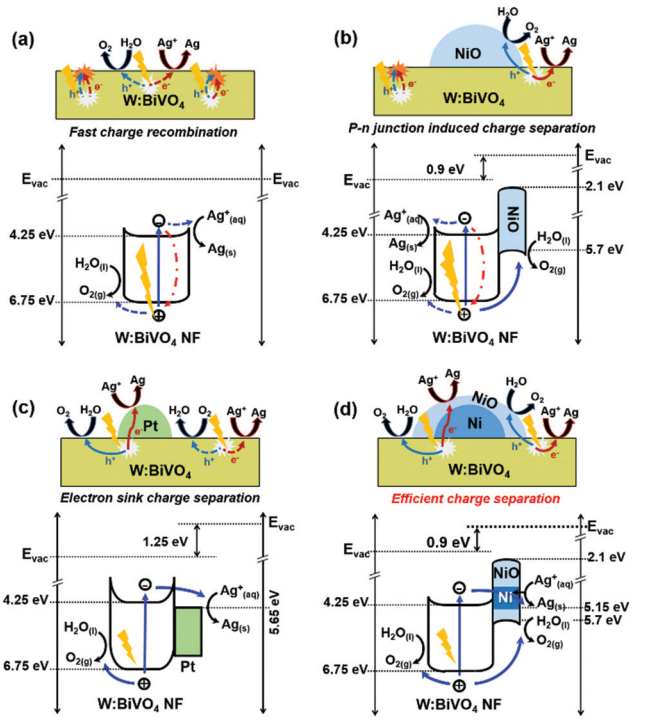

Fig. 4 The proposed mechanism of photocatalytic water oxidation of (a) pristine, (b) NiO-loaded, (c) Pt-loaded, and (d) Ni@NiO-loaded W:$BiVO_4$ NFs in aqueous silver nitrate solution (50 mM). The electronic affinity of W:$BiVO_4$ and NiO are 4.25 eV and 2.1 eV,[26] and the work functions of Ni and Pt are 5.15 eV [24] and 5.65 eV,[25] respectively.

(Fig. 4c). This supposition can be equally applied in the case of Ni@NiO/W:$BiVO_4$ NFs. The photogenerated electrons in W:$BiVO_4$ NFs tend to transfer to the Ni metal existing at the interface of W:$BiVO_4$ and NiO shell due to the potential gradient (ΔE = 0.9 eV) raised from the difference between the work function of Ni (5.15 eV)[24] and the electron affinity of W:$BiVO_4$ (4.25 eV) (Fig. 4d). Therefore, the photogenerated holes can easily migrate to the valence band of W:$BiVO_4$, resulting in an effective charge separation in W:$BiVO_4$ NFs. Considering the work functions of Pt (5.65 eV),[25] Pt has been known to be more effective than metallic Ni in terms of electron scavenging. However, Ni@NiO/W:$BiVO_4$ NFs showed a better performance than that of Pt/W:$BiVO_4$ NFs. This result clearly shows that Ni@NiO came into contact with the W:$BiVO_4$ NFs which has an important function in the activity. As described in Fig. 4d, the fast electron injection into the core Ni metal can suppress the EHP recombination, thus the residual holes on the surface of W:$BiVO_4$ could involve the water oxidation reaction effectively. In addition to this, the photogenerated holes would diffuse to the NiO on the surface of Ni@NiO/W:$BiVO_4$ NFs due to the band bending, and they take part in the water oxidation reaction.

To estimate the external quantum efficiency of W:$BiVO_4$ particles, W:$BiVO_4$ NFs, and 0.1Ni@NiO/W:$BiVO_4$ NFs, a photocatalytic water oxidation reaction characteristic was investigated using blue light-emitting diodes (Fig. S14†). The

external quantum efficiencies (EQE, η), defined by eqn (1) shown in the Experimental section, were calculated to be 1.37, 3.18, and 5.84 for the W:$BiVO_4$ particles, W:$BiVO_4$ NFs, and 0.1Ni@NiO/W:$BiVO_4$ NFs, respectively. The significant enhancement in EQE for 0.1Ni@NiO/W:$BiVO_4$ NFs was closely related to the fact that 0.1Ni@NiO/W:$BiVO_4$ NFs exhibited a higher O_2 evolution rate (3.43 μmol h^{-1}) than those of W:$BiVO_4$ particles (1.04 μmol h^{-1}) and W:$BiVO_4$ NFs (2.54 μmol h^{-1}). The result demonstrates that remarkably improved photocatalytic water oxidation of Ni@NiO/W:$BiVO_4$ NFs is obtained by the synergetic effects including increased surface area of electrospun W:$BiVO_4$ NFs and the rational combination with bi-functional Ni@NiO co-catalysts for an effective photocatalytic reaction.

Conclusions

Highly porous W:$BiVO_4$ NFs have been successfully synthesized *via* facile electrospinning and a subsequent calcination process. In addition, an earth-abundant Ni co-catalyst was introduced as a form of Ni@NiO *via* an Ar ambient annealing step. The Ni@NiO/W:$BiVO_4$ NFs exhibited significantly improved water oxidation performance under visible light irradiation compared with those of Pt- or NiO NPs-loaded W:$BiVO_4$ NFs. In detail, the porous W:$BiVO_4$ NFs provide numerous reaction sites and partially oxidized Ni@NiO NPs serve as electron sinks (Ni core) by electronic band bending as well as the additional water oxidation sites (NiO shell), simultaneously. Our synthetic strategy can be extended to other possible combinations of earth-abundant and efficient catalysts in an effort to provide an improved performance by the synergetic effect.

Acknowledgements

This work was supported by the National Research Foundation (NRF) *via* the National Research Laboratory (NRL) (R0A-2008-000-20041-0), the Converging Research Center (2009-0082276), the Engineering Research Center (2012-0001175) Programs, and the Saudi Aramco – KAIST CO_2 Management Center. This work was also supported by the Korea CCS R&D Center (KCRC) grant funded by the Korea government (Ministry of Science, ICT & Future Planning) (no. NRF-2014M1A8A1049303).

Notes and references

1 (*a*) N. S. Lewis and D. G. Nocera, *Proc. Natl. Acad. Sci. U. S. A.*, 2006, **103**, 15729; (*b*) N. S. Lewis, *Science*, 2007, **315**, 798.

2 (*a*) A. Fujishima and K. Honda, *Nature*, 1972, **238**, 37; (*b*) S. S. Mao and S. H. Shen, *Nat. Photonics*, 2013, **7**, 944.

3 (*a*) K. Maeda, *J. Photochem. Photobiol., C*, 2011, **12**, 237; (*b*) J. W. Sun, D. K. Zhong and D. R. Gamelin, *Energy Environ. Sci.*, 2010, **3**, 1252; (*c*) J. Augustynski, B. D. Alexander and R. Solarska, *Top. Curr. Chem.*, 2011, **303**, 1.

4 (*a*) M. G. Walter, E. L. Warren, J. R. McKone, S. W. Boettcher, Q. X. Mi, E. A. Santori and N. S. Lewis, *Chem. Rev.*, 2011, **111**, 5815; (*b*) R. Abe, *J. Photochem. Photobiol., C*, 2010, **11**, 179; (*c*) A. Kudo and Y. Miseki, *Chem. Soc. Rev.*, 2009, **38**, 253; (*d*) J. Li, W. Zhao, Y. Guo, Z. Wei, M. Han, H. He, S. Yang and C. Sun, *Appl. Surf. Sci.*, 2015, **351**, 270.

5 (*a*) A. Kudo, K. Ueda, H. Kato and I. Mikami, *Catal. Lett.*, 1998, **53**, 229; (*b*) S. Tokunaga, H. Kato and A. Kudo, *Chem. Mater.*, 2001, **13**, 4624.

6 (*a*) W. J. Jo, J. W. Jang, K. J. Kong, H. J. Kang, J. Y. Kim, H. Jun, K. P. Parmar and J. S. Lee, *Angew. Chem., Int. Ed.*, 2012, **51**, 3147; (*b*) S. K. Choi, W. Choi and H. Park, *Phys. Chem. Chem. Phys.*, 2013, **15**, 6499; (*c*) L. Tong, A. Iwase, A. Nattestad, U. Bach, M. Weidelener, G. Gotz, A. Mishra, P. Bauerle, R. Amal, G. G. Wallace and A. J. Mozer, *Energy Environ. Sci.*, 2012, **5**, 9472.

7 (*a*) Z. Q. Wang, W. J. Luo, S. C. Yan, J. Y. Feng, Z. Y. Zhao, Y. S. Zhu, Z. S. Li and Z. G. Zou, *CrystEngComm*, 2011, **13**, 2500; (*b*) D. E. Wang, H. F. Jiang, X. Zong, Q. A. Xu, Y. Ma, G. L. Li and C. Li, *Chem. – Eur. J.*, 2011, **17**, 1275; (*c*) D. N. Ke, T. Y. Peng, L. Ma, P. Cai and P. Jiang, *Appl. Catal., A*, 2008, **350**, 111; (*d*) J. Yu, Y. Zhang and A. Kudo, *J. Solid State Chem.*, 2009, **182**, 223.

8 Y. H. Ng, A. Iwase, A. Kudo and R. Amal, *J. Phys. Chem. Lett.*, 2010, **1**, 2607.

9 Y. Park, K. J. McDonald and K. S. Choi, *Chem. Soc. Rev.*, 2013, **42**, 2321.

10 (*a*) F. F. Abdi, N. Firet and R. V. D. Krol, *ChemCatChem*, 2013, **5**, 490; (*b*) D. K. Zhong, S. Choi and D. R. Gamelin, *J. Am. Chem. Soc.*, 2011, **133**, 18370; (*c*) W. Yao, H. Iwai and J. Ye, *Dalton Trans.*, 2008, 1426; (*d*) H. Ye, J. Lee, J. S. Jang and A. J. Bard, *J. Phys. Chem. C*, 2010, **114**, 13322.

11 (*a*) L. Ge, *J. Mol. Catal. A: Chem.*, 2008, **282**, 62; (*b*) L. Ge, *Mater. Lett.*, 2008, **62**, 926; (*c*) A. Zhang and J. Zhang, *Appl. Surf. Sci.*, 2010, **256**, 3224; (*d*) S. W. Cao, Z. Yin, J. Barber, F. Y. Boey, S. C. Loo and C. Xue, *ACS Appl. Mater. Interfaces*, 2012, **4**, 418; (*e*) C. N. Van, W. S. Chang, J. W. Chen, K. A. Tsai, W. Y. Tzeng, Y. C. Lin, H. H. Kuo, H. J. Liu, K. D. Chang, W. C. Chou, C. L. Wu, Y. C. Chen, C. W. Luo, Y. J. Hsu and Y. H. Chu, *Nano Energy*, 2015, **15**, 625.

12 (*a*) S. K. Pilli, T. E. Furtak, L. D. Brown, T. G. Deutsch, J. A. Turner and A. M. Herring, *Energy Environ. Sci.*, 2011, **4**, 5028; (*b*) Q. Jia, K. Iwashina and A. Kudo, *Proc. Natl. Acad. Sci. U. S. A.*, 2012, **109**, 11564; (*c*) H. W. Jeong, T. H. Jeon, J. S. Jang, W. Choi and H. Park, *J. Phys. Chem. C*, 2013, **117**, 9104; (*d*) J. A. Seabold and K. S. Choi, *J. Am. Chem. Soc.*, 2012, **134**, 2186; (*e*) H. Ye, H. S. Park and A. J. Bard, *J. Phys. Chem. C*, 2011, **115**, 12464; (*f*) D. Wang, R. Li, J. Zhu, J. Shi, X. Zong and C. Li, *J. Phys. Chem. C*, 2012, **116**, 5082; (*g*) H. Li, H. Yu, X. Quan, S. Chen and H. Zhao, *Adv. Funct. Mater.*, 2015, **25**, 3074.

13 (*a*) K. Domen, A. Kudo and T. Onishi, *J. Phys. Chem.*, 1986, **90**, 292; (*b*) L. Guo, H. Hagiwara, S. Ida, T. Daio and

T. Ishihara, *ACS Appl. Mater. Interfaces*, 2013, **5**, 11080; (*c*) M. Yabuta, T. Takayama, K. Shirai, K. Watanabe, A. Kudo, T. Sugimoto and Y. Matsumoto, *J. Phys. Chem. C*, 2014, **118**, 10972; (*d*) M. T. McDowell, M. F. Lichterman, J. M. Spurgeon, S. Hu, I. D. Sharp, B. S. Brunschwig and N. S. Lewis, *J. Phys. Chem. C*, 2014, **118**, 19618.

14 F. E. Osterloh, *Chem. Soc. Rev.*, 2013, **42**, 2294.

15 (*a*) X. Wang, G. Li, J. Ding, H. Peng and K. Chen, *Mater. Res. Bull.*, 2012, **47**, 3814; (*b*) J. Yu and A. Kudo, *Adv. Funct. Mater.*, 2006, **16**, 2163; (*c*) Y. K. Kho, W. Y. Teoh, A. Iwase, L. Madler, A. Kudo and R. Amal, *ACS Appl. Mater. Interfaces*, 2011, **3**, 1997.

16 (*a*) W. Liu, Y. Yu, L. Cao, G. Su, X. Liu, L. Zhang and Y. Wang, *J. Hazard. Mater.*, 2010, **181**, 1102; (*b*) L. Ren, L. Ma, L. Jin, J. B. Wang, M. Qiu and Y. Yu, *Nanotechnology*, 2009, **20**, 405602; (*c*) Y. Zhou, K. Vuille, A. Heel, B. Probst, R. Kontic and G. R. Patzke, *Appl. Catal., A*, 2010, **375**, 140.

17 Y. Cheng, J. Chen, X. Yan, Z. Zheng and Q. Xue, *RSC Adv.*, 2013, **3**, 20606.

18 G. G. Couto, J. J. Klein, W. H. Schreiner, D. H. Mosca, A. J. D. Oliveira and A. J. Zarbin, *J. Colloid Interface Sci.*, 2007, **311**, 461.

19 J. Xiao and S. Yang, *J. Mater. Chem.*, 2012, **22**, 12253.

20 (*a*) K. M. Young and T. W. Hamann, *Chem. Commun.*, 2014, **50**, 8727; (*b*) L. Trotochaud, J. K. Ranney, K. N. Williams and S. W. Boettcher, *J. Am. Chem. Soc.*, 2012, **134**, 17253.

21 A. Kudo, K. Omori and H. Kato, *J. Am. Chem. Soc.*, 1999, **121**, 11459.

22 (*a*) A. Singh, S. L. Y. Chang, R. K. Hocking, U. Bach and L. Spiccia, *Energy Environ. Sci.*, 2013, **6**, 579; (*b*) K. Fominykh, J. M. Feckl, J. Sicklinger, M. Doblinger, S. Bocklein, J. Ziegler, L. Peter, J. Rathousky, E. W. Scheidt, T. Bein and D. Fattakhova-Rohlfing, *Adv. Funct. Mater.*, 2014, **24**, 3123.

23 J. Yang, D. Wang, H. Han and C. Li, *Acc. Chem. Res.*, 2012, **46**, 1900.

24 A. Kumatani, Y. Li, P. Darmawan, T. Minari and K. Tsukagoshi, *Sci. Rep.*, 2013, **3**, 1026.

25 D. F. Gu, S. K. Dey and P. Majhi, *Appl. Phys. Lett.*, 2006, **89**, 082907.

26 K. X. Steirer, P. F. Ndione, N. E. Widjonarko, M. T. Lloyd, J. Meyer, E. L. Ratcliff, A. Kahn, N. R. Armstrong, C. J. Curtis, D. S. Ginley, J. J. Berry and D. C. Olson, *Adv. Energy Mater.*, 2011, **1**, 813.